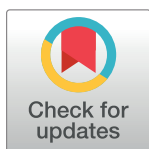# Temperature and concentration calibration of aqueous polyvinylpyrrolidone (PVP) solutions for isotropic diffusion MRI phantoms

Friedrich Wagner[1], Frederik B. Laun[1,2], Tristan A. Kuder[1], Anna Mlynarska[3], Florian Maier[1], Jonas Faust[1], Kerstin Demberg[1], Linus Lindemann[1], Boris Rivkin[1], Armin M. Nagel[1,2], Mark E. Ladd[1], Klaus Maier-Hein[4], Sebastian Bickelhaupt[3], Michael Bach[1] *

1 Medical Physics in Radiology, German Cancer Research Center (DKFZ), Heidelberg, Germany, **2** Institute of Radiology, University Hospital Erlangen, Erlangen, Germany, **3** Radiology, German Cancer Research Center (DKFZ), Heidelberg, Germany, **4** Medical and Biological Informatics, German Cancer Research Center (DKFZ), Heidelberg, Germany

* m.bach@dkfz.de

Abbreviations: b, b-value; c_{PVP}, concentration of PVP in % (weight/weight); D_{app}, apparent diffusion

Abstract

To use the "apparent diffusion coefficient" (D_{app}) as a quantitative imaging parameter, well-suited test fluids are essential. In this study, the previously proposed aqueous solutions of polyvinylpyrrolidone (PVP) were examined and temperature calibrations were obtained. For example, at a temperature of 20˚C, D_{app} ranged from 1.594 (95% CI: 1.593, 1.595) µm^2/ms to 0.3326 (95% CI: 0. 3304, 0.3348) µm^2/ms for PVP-concentrations ranging from 10% (w/w) to 50% (w/w) using K30 polymer lengths. The temperature dependence of D_{app} was found to be so strong that a negligence seems not advisable. The temperature dependence is descriptively modelled by an exponential function $\exp(c_2 (T - 20˚C))$ and the determined c_2 values are reported, which can be used for temperature calibration. For example, we find the value 0.02952 K^{-1} for 30% (w/w) PVP-concentration and K30 polymer length. In general, aqueous PVP solutions were found to be suitable to produce easily applicable and reliable D_{app}-phantoms.

Introduction

Diffusion weighted imaging (DWI) is a magnetic resonance imaging (MRI) technique that finds widespread application today [1–4]. By means of diffusion-weighting magnetic field gradient pulses [5], the diffusion of water in human tissue can be measured in a spatially resolved manner thus yielding, for example, maps of the apparent diffusion coefficient [1]. Cellular structures restrict the diffusive motion, which allows inferring information about structural properties of cells and tissue. This can be exploited, for example, to depict the course of white matter tracts in the human brain by measuring anisotropic diffusion with diffusion tensor imaging (DTI) [6] and with fiber tracking [7, 8]. More advanced methods like q-ball imaging [9] and diffusion kurtosis imaging [10] extend the diffusion tensor approach making possible the detection of fiber crossings and the detection of non-Gaussian diffusion properties.

coefficient; DWI, diffusion weighted imaging; MRI, magnetic resonance imaging; PVP, polyvinylpyrrolidone; T, temperature.

As DWI is a sensitive technique, several approaches for validation using ground truth phantoms have been proposed. On the one hand, phantoms mimicking anisotropic diffusion of neuronal tissue have been proposed. These phantoms are often made using thin fibers that make the diffusive motion of the fiber-embedding fluid anisotropic. Such phantoms have been used for multiple different methodological developments in the fields of diffusion tensor imaging [11–21], kurtosis tensor imaging [12, 22], q-ball imaging [20, 21, 23–26], tract-based spatial statistics [27], and fiber tracking [13, 20, 28]. Besides the development of advanced DWI methods, also the quality and repeatability [16] was assessed with such phantoms as well as the comparability of tensor metrics in a multi-center study [29]. Moreover, phantoms consisting of hollow fibers and capillaries have been proposed and were applied successfully (e.g. [30–34]).

Stepping back from these advanced applications, an increased interest has recently sparked in finding good isotropic diffusion phantoms. While water has been used in a majority of cases [35–40], it has some drawback such as a low viscosity, which may result in non-negligible fluid convection, or a diffusion coefficient that is much higher than that of typical human tissues and lesions. Consequently, a number of further test fluids has been proposed such as cyclohexane [41, 42], dioxane [41], DMSO [41], pentanol [41], sucrose [43], ethylene Glycol [44], cyclohexane [45], cycloheptane [42, 45], cyclooctane [42, 45], n-octane to n-hexadecane [41, 42], ethanol [42], n-propanol [42], n-butanol [42], and aqueous solutions of polyvinylpyrrolidone (PVP) [46–50]. Applications included quality control examinations and investigations of precision and accuracy [35, 45, 51, 52], evaluations of gradient performance [44], sequence evaluation [46].

One issue with all test fluids is that their diffusion properties depend on their temperature. One possibility is to fix the temperature, for example, by putting the test fluid in ice water thus maintaining a constant temperature of 0°C [38, 39, 51]. The other approach is to correct the measured diffusion coefficients to a reference temperature using calibration curves [35, 36, 41, 42, 44, 45]. As PVP solutions have many favorable properties, which comprise a concentration-adjustable water diffusion coefficient and an increased viscosity of the fluid, the aim of this work was to provide the calibration curves for two common PVP polymer chain lengths for typical bore temperature of clinical whole body MR scanners.

Material and methods

Phantom

Nine plastic tubes (volume 50 ml) were filled with aqueous solutions of polyvinylpyrrolidone (PVP) (AppliChem GmbH, Darmstadt, Germany, K30 with 44–55 kg/mol and K90 with 1,000–1,500 kg/mol) with concentrations c_{PVP} of 10, 20, 30, 40, and 50% for K30 and 10, 20, and 30% for K90 (w/w). Concentrations of K90 of 40% and 50% were not used, since these concentrations resulted in fluids of high viscosity with trapped air bubbles. The tubes were immersed in a water-filled closed bin, which was placed in a surrounding water bath (Fig 1) to fill the used receive coil to a maximal extent. The temperature was recorded using a fiber optical thermometer (Luxtron FOT Lab Kit, LumaSense Technologies, CA, USA) in intervals of approximately 1 s at three positions: In the central water-filled tube, in the bin and in the surrounding water bath (see red crosses in Fig 1). The temperature of the central water-filled probe was used; the other two probes were used for an additional verification. Moreover, the recorded temperature was averaged over the scan time of each measurement sequence. The vendor provided accuracy is ±0.5°C within 50°C of the calibration temperature, ±0.2°C within 20°C of calibration temperature, and ±0.1°C at calibration temperature. The phantom was calibrated with a one-point temperature calibration using an ice-water bath before each measurement series. Verification exams of the Luxtron thermometer revealed a temperature offset of
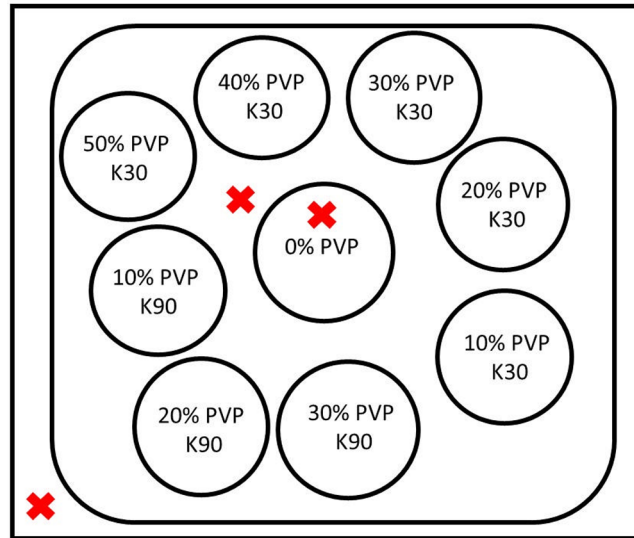
Fig 1. (single column). Sketch of the phantom. Tubes with different PVP solutions were contained in a water-filled bin, which was itself immersed in a water bath. Temperature was recorded at three positions (red crosses).

approximately +0.9˚C (see supplemental material S1 File). The recorded temperature values were thus corrected by subtracting this offset.

MRI experiments

MRI experiments were performed on a 1.5 T scanner (Magnetom Aera, Siemens Healthcare, Erlangen, Germany) using a 20-channel head-coil and on a 3.0 T scanner (Magnetom Prisma fit, Siemens Healthcare, Erlangen, Germany) using a 64-channel head coil. A diffusion-weighted echo planar imaging sequence was used and data was acquired with two parameters sets:

1. High resolution parameter set: repetition time TR = 5000 ms, echo time TE = 144 ms, readout bandwidth = 1000 Hz/px, field of view = 200 x 200 mm^2, 20 slices, voxel size = 1 x 1 x 5 mm^3, parallel imaging with GRAPPA and acceleration factor of 2, three orthogonal, monopolar diffusion weightings, strength of diffusion weighting b = 0, 100, 200, 300, 400, 500, 600, and 700 s/mm^2 acquired with 1 average (b = 0 s/mm^2), 2 averages (b = 100 to 500 s/mm^2), or three averages (b = 600 and 700 s/mm^2), magnitude images were averaged, the vendor-provided image filter was set to "strong" to suppress Gibbs ringing. Acquisition time was 5:52 min.

2. Low resolution parameter set: Identical parameters as for the high resolution parameter set except for: TE = 86 ms, voxel size = 2 x 2 x 5 mm^3.

The tubes were oriented perpendicular to the main magnetic field, i.e. along the anterior-posterior direction, and the image plane was coronal, i.e. perpendicular to the tubes. High and low resolution datasets were acquired alternatingly. A low duty cycle sequence of 8:22 min was inserted between them to avoid potential heating of the gradient system.

Four data acquisition series were run at each scanner. Two times, the phantom was warmed up to about 30˚ and was let to cool down. Two times, the phantom was cooled to about 14˚C and was let to warm up. Each of the series was acquired in an overnight scan lasting about 10

to 12 hours. One temperature recording file of a 3.0 T run was corrupted so that this run was excluded from the analysis.

Data evaluation

Apparent diffusion coefficients (D_{app}) were computed for each voxel using the equation

$$S(b) = S_0 \exp(-bD_{app}), \tag{1}$$

where $S(b)$ is the signal intensity in dependence of the b-value with the free fit parameters S_0 and D_{app} [5, 6]. Mean D_{app}-values were computed for manually drawn volumes of interest (VOIs). The circular cross section was specified on the images within the tubes with a safety margin of roughly 3 mm to the tube boundary (see Fig 2). In slice direction, the VOIs encompassed 5 or 6 adjacent slices. VOIs were drawn such that regions of increased distortions at the edges of the tubes were spared. The diffusion weighted maps were inspected visually to avoid regions with other potential artifacts.

The dependency of D_{app} on the temperature T was descriptively modelled by the equation

$$D_{app} = c_1 \cdot \exp(c_2 \cdot (T - T_0)). \tag{2}$$

Here, c_1 is the apparent diffusion coefficients at $T_0 = 20°C$ and c_2 describes the temperature dependence. Eqs 1 and 2 were fitted using the Levenberg-Marquardt algorithm thus determining D_{app} and S_0 (not used in further calculation) in Eq 1, and c_1 and c_2 in Eq 2. 95% confidence intervals were computed.

The dependence of c_2 on c_{PVP} was modelled by means of a linear fit according to the equation

$$c_2 = a_{c_2} + b_{c_2} \cdot c_{PVP} \tag{3}$$

The coefficients a_{c_2} and b_{c_2} were determined by means of a linear least square fit using the values determined for c_2 with fitting weights equal to the inverse of the 95% confidence intervals. Additionally, aiming at a further increase of accuracy, the value for c_2 at $c_{PVP} = 0$ from Mill et al. [53] was included in the fit with a fitting weight equal to the average weight of the other data points.

An estimate of the signal to noise ratio (SNR) was obtained by dividing the signal in the PVP solution by the signal in a region of interest outside the phantom. One has to note that this estimate has to be considered being far from accurate, in part due to the use of parallel imaging.

Results

An image slice of the phantom is shown in Fig 2 for one high and one low resolution image set acquired at 1.5 T. Images acquired with $b = 0$ s/mm^2 (Fig 2a and 2d), with $b = 700$ s/mm^2 (Fig 2b and 2e), and maps of D_{app} (Fig 2c and 2f) are shown. A negative correlation between PVP concentration and D_{app} is observed in the D_{app}-maps. In the $b = 700$ s/mm^2 images, higher PVP concentrations are reflected by a reduced signal drop. The estimated SNR ranged from 40 to 140 in the $b = 0$ images.

Fig 3 shows the dependency of D_{app} on the temperature T for K30 and for K90. Fits of Eq (2) are shown as black lines and are generally in good accordance with the measured data. The data of the seven displayed acquisition runs are generally also in good agreement, but few outlier runs are present, e.g. for water and for K30 with $c_{PVP} = 50\%$. Tables 1 and 2 provide the fitted parameters c_1 and c_2. The differences of the fit-parameters between the two K-values at
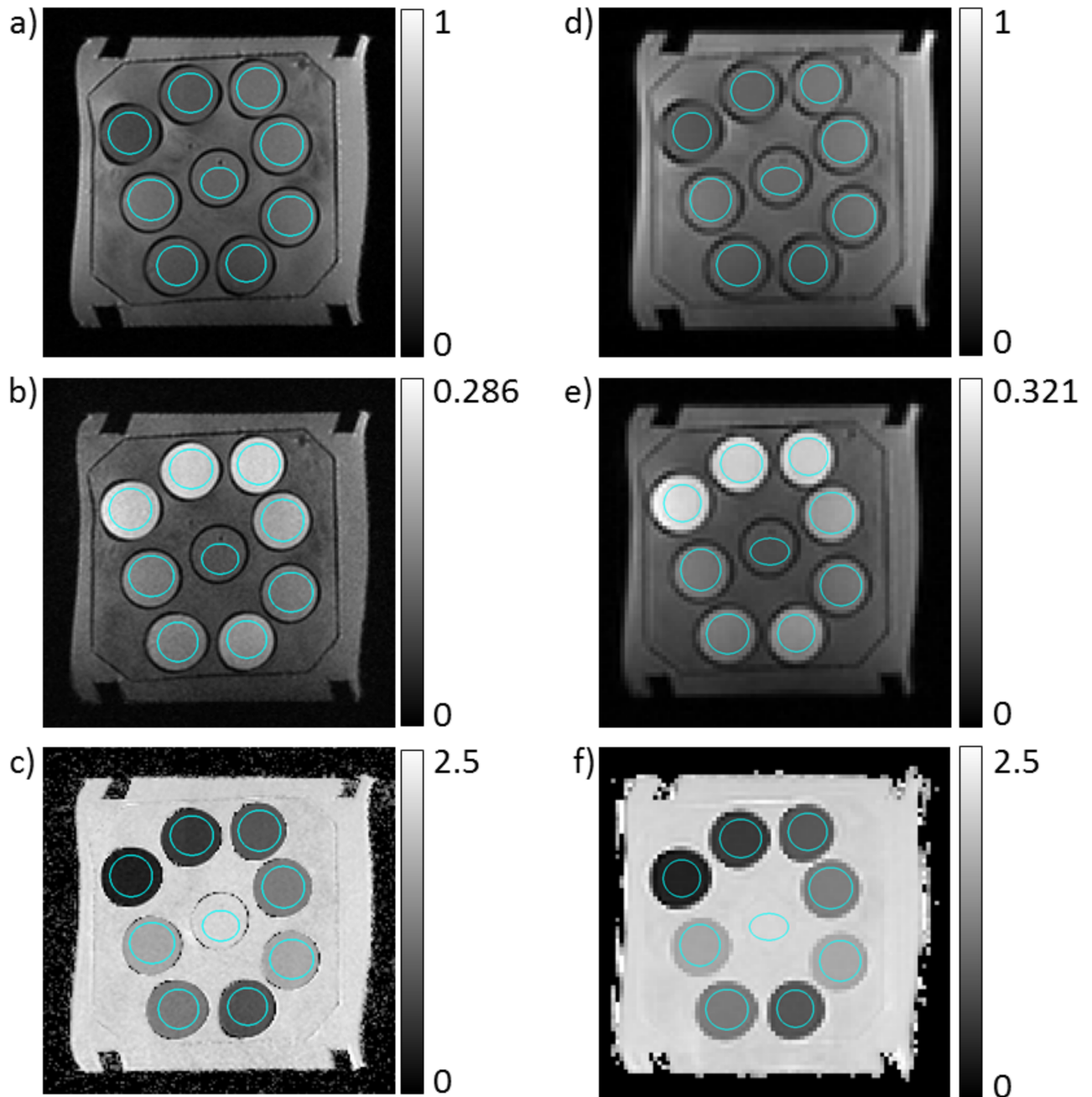
Fig 2. (double column): Images of the used phantom. a,b,c) High resolution images. d,e,f) Low resolution images. a,d) Signal images without diffusion weighting, i.e. with $b = 0$ s/mm^2. b,e) Signal image with $b = 700$ s/mm^2. Signal images are min-max normalized. c,f) D_{app}-maps of the phantom in units of μm^2/ms. Cross sections of the volumes of interest are marked in blue in a and d.

https://doi.org/10.1371/journal.pone.0179276.g002

one specific temperature are rather low. Parameters c_1 and c_2 that were determined only with the 1.5T scanner, or with the 3.0T scanner, are provided as supplemental material S2 File.

Fig 4 shows c_2 in dependence of c_{PVP}. The straight lines represent Eq (3), i.e. a linear interpolation. The coefficients are $a_{c_2} = 0.0244$ K^{-1} and $b_{c_2} = 1.7011 \cdot 10^{-4}$ K^{-1}/%(w/w) for K30 and $a_{c_2} = 0.0246$ K^{-1} and $b_{c_2} = 9.772 \cdot 10^{-5}$ K^{-1}/%(w/w) for K90. The data points do not lie perfectly
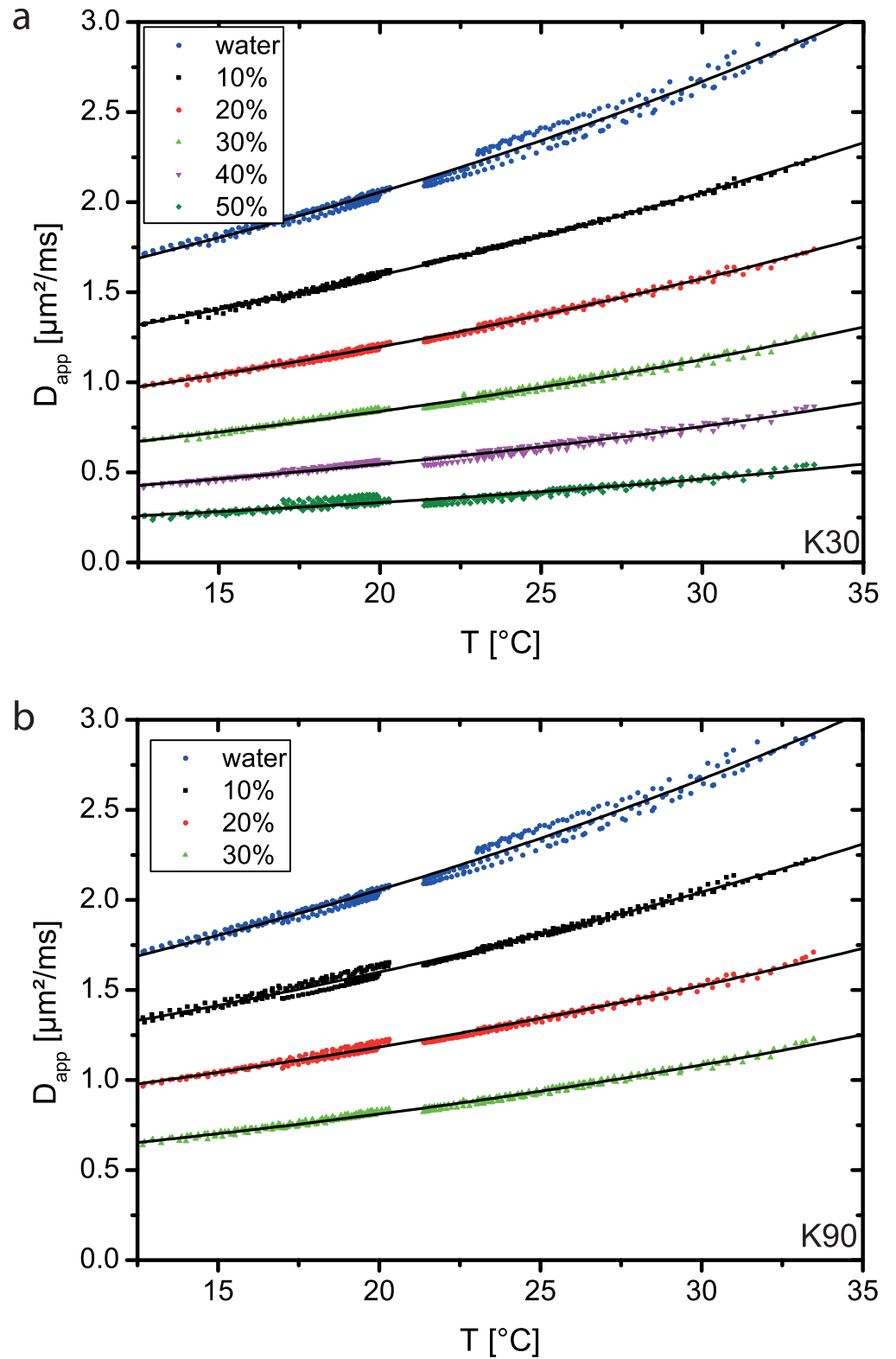
Fig 3. (single column): Dependence of apparent diffusion coefficient D_{app} on temperature for K30 and K90. Markers represent measured values and lines represent fits according to Eq 2.

https://doi.org/10.1371/journal.pone.0179276.g003

Table 1. Fit parameters describing the dependency of D_{app} on the temperature (see Eq (2)) for K30. 95% confidence intervals are stated in brackets.

c_{PVP} [% (w/w)]	c_1 [μm²/ms]	c_2 [1/K]
0	2.055 (2.050, 2.059)	0.02617 (0.02583, 0.02652)
10	1.594 (1.593, 1.595)	0.02531 (0.02519, 0.02542)
20	1.197 (1.195, 1.198)	0.02749 (0.02729, 0.02769)
30	0.8388 (0.8372, 0.8403)	0.02952 (0.02921, 0.02983)
40	0.5465 (0.5447, 0.5482)	0.03247 (0.03194, 0.03299)
50	0.3326 (0.3304, 0.3348)	0.03303 (0.03197, 0.03409)
0 (Data by Mills, determined using T = 15, 25, and 35°C)	2.02 (1.864, 2.176)	0.02466 (0.01777, 0.03155)

https://doi.org/10.1371/journal.pone.0179276.t001

Table 2. Fit parameters describing the dependency of D_{app} on the temperature (see Eq (2)) for K90. 95% confidence intervals are stated in brackets.

c_{PVP} [% (w/w)]	c_1 [μm²/ms]	c_2 [1/K]
10	1.599 (1.596, 1.601)	0.02453 (0.02428, 0.02479)
20	1.183 (1.181, 1.185)	0.02536 (0.0251, 0.02563)
30	0.8112 (0.8096, 0.8128)	0.02893 (0.02861, 0.02925)

https://doi.org/10.1371/journal.pone.0179276.t002

on the interpolating straight line. If the assumption that the relation between c_2 and c_{PVP} is linear is correct, then the linear interpolation presumably averages out experimental errors and hence it would be more advisable to use the c_2 values predicted by the interpolation. These values are stated in Table 3.

Discussion

The here provided data can be used to calibrate measurements to the sample temperature. Measurements without temperature calibration or temperature fixation seem not advisable, because the observed temperature dependency appears too strong to be acceptable.

For the case of water, the obtained coefficients c_1 and c_2 are in good keeping with published values. For example, using our measured c_1 and c_2 in Table 1 for free water, one obtains diffusion coefficients estimated at temperatures 15°C, 25°C, and 35° of 1.819 μm²/ms, 2.322 μm²/ms, and 2.963 μm²/ms. This matches, for example, closely to the values published by Mills, which are 1.777 μm²/ms, 2.299 μm²/ms and 2.919 μm²/ms [53]. Pullens et al. and Pierpaoli et al. published values for K30 at 21°C and at 22°C, but used the unit weight per volume (w/v). At 30% w/v, Pullens et al. obtained a D_{app} of approximately 0.852 μm²/ms at 21°C, and Pierpaoli et al. obtained approximately 0.955 μm²/ms at 22°C. Our values for c_1 and c_2 predict 0.960 μm²/ms at 21°C and 0.983 μm²/ms at 22°C taking into account the difference between (w/w) and (w/v) by means of linear interpolation and using calibration curves that we obtained (K30: $c_{PVP(w/v)} = 1.0955 c_{PVP(w/w)}$. K90: $c_{PVP(w/v)} = 1.0535 c_{PVP(w/w)}$): We found that 30% (w/v) corresponds to 27.4% (w/w) for K30 (see supplemental material S2 File) and used this value for calculation of D_{app}. Thus our values are closer to those reported by Pierpaoli et al. with a difference of about 3%. Keenan et al. have reported diffusion coefficients for different PVP concentrations [48]. They used a slightly different polymer weight, but given the little difference of the coefficients $c1$ and $c2$ between K30 and K90 despite a vastly different typical molecular weight, it seems reasonable to compare their values to our K30 values. Keenan et al. report for 10% w/w that D_{app} ranges from 1.536 μm²/ms at 17.91°C to 1.714 μm²/ms at 22.11°C,
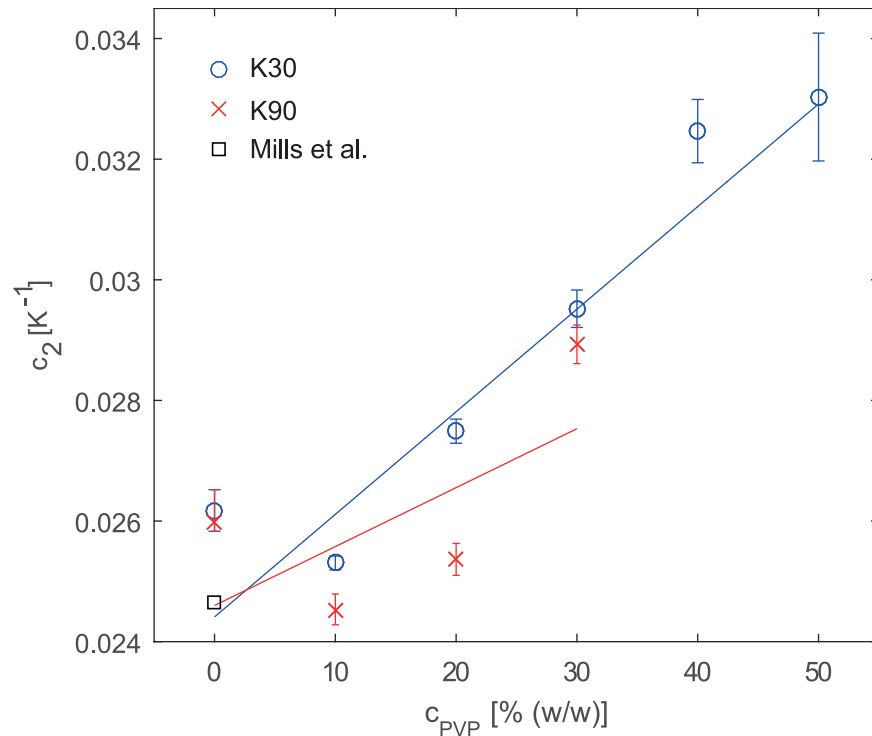
Fig 4. (single column): Temperature calibration coefficient c_2 in dependence of PVP concentration for K30 and K90. Error bars denote 95% confidence intervals. The straight lines represent linear fits with weights inversely proportional to the width of the 95% confidence interval.

https://doi.org/10.1371/journal.pone.0179276.g004

while we find corresponding values of 1.509 µm^2/ms to 1.684 µm^2/ms. At 40% (w/w), Keenan et al. report that D_{app} ranges from 0.557 µm^2/ms at 17.91˚C to 0.640 µm^2/ms at 22.11˚C, while we find corresponding values of 0.512 µm^2/ms to 0.584 µm^2/ms. Thus at lower concentrations, a good agreement is observed, but at larger concentrations, the deviation becomes as large as 10%. One explanation might be that PVP is hygroscopic (maximal water content of 5% according to vendor). Thus the weight of the powder can depend on its water content. Potentially, this must be accounted for when using PVP solutions as a DWI reference standard. Interestingly, however, the ratio between D_{app} values at the largest and the smallest temperature is 0.640/0.557≈1.149 for Keenan et al.'s values and 0.584/0.512≈1.141 for our values indicating that the c_2-based calibration by Eq (2) would be in good keeping with what one would expect using Keenan et al.'s values.

Table 3. Recommended temperature calibration coefficient c_2 in K^{-1}.

c_{PVP} [% (w/w)]	K30	K90
0	0.0244	0.0246
10	0.0261	0.0256
20	0.0278	0.0266
30	0.0295	0.0275
40	0.0312	
50	0.0329	

https://doi.org/10.1371/journal.pone.0179276.t003

In comparison to other proposed test fluids, aqueous solutions of PVP have several advantages: First, multiple image ghosts arising from chemical shifts are not observed in the echo planar data, which would be the case, e.g., using other proposed test fluids as ethanol or n-propanol [42]. Second, the water diffusivity can be adjusted specifically to desired values by changing the PVP concentration, which is not possible, e.g. using cyclo-alkanes [41, 42, 45]. Third, one measures water protons and not protons bound to other molecules as for most of the other test fluids. As the Larmor frequency of the water protons in the PVP solution is close to the water frequency in pure water, fat suppression techniques can be tested conveniently when adding a fat containing volume to the phantom. This would be difficult, e.g., using ethanol. Fourth, unlike ethanol and alkanes, aqueous PVP solutions are not flammable. Fifth, PVP has a mono-exponential signal decay with respect to b and, sixth, it is independent of diffusion time [49]. Seventh, PVP solutions have a higher viscosity than pure water, which prevents fluid convection and hence increases measurement accuracy and precision. Very high PVP concentrations are, however, hard to work with, which might explain the outliers observed for $c_{PVP} = 50\%$. Moreover, high PVP concentrations are more likely to contain air pockets. In particular, the K90 solutions with $c_{PVP} = 30\%$ appear to us to be potentially outside the trustable range due their very high viscosity and thus difficult handling. One drawback of PVP solutions is their susceptibility to mold and bacteria growth, which they have in common with many gels [54]. This can, however, be overcome by adding preservatives like sodium azide [47, 49]. One further property of increased PVP concentrations is the reduced T_1 time [48, 55].

A recently proposed alternative test fluid is decamethylcyclopentasiloxane [56]. It shares some of the advantageous properties of PVP, such as non-toxicity, a single chemical shift line and mono-exponential signal decay. Its diffusion coefficient is smaller by roughly a factor of 10 compared to water, which can be an advantage in applications involving strong diffusion weightings. A drawback is that the diffusion coefficient cannot be adjusted as for aqueous PVP solutions by changing PVP concentration. Moreover it has a different chemical shift than water protons making it potentially difficult to assess fat saturation techniques.

A drawback of the current study is that the calibration curves were obtained with systems that have, of course, their own systematic errors. This was partly overcome by using two systems and several acquisition series. However, in order to perform a temperature calibration, one does not necessarily have to rely on the absolute D_{app} values being correct. Only the relative change with temperature, i.e. c_2, must be known.

A further limitation is that the test tubes did only cover a limited space. Thus one must rely on the assumption that the measured D_{app} value shows little spatial variation and that ringing artifacts can be neglected (see supplemental material S4 File for an assessment of Gibbs ringing). Moreover, the rather complicated structure of the measurement setup is not ideal to acquire echo planar images. A more suitable setup addressing these two issues would have been the consecutive measurement of the different PVP solutions in spherical bins; but owing to the arising large demands on acquisition time, the more practical approach of combing all PVP solutions in a single phantom was used in this work. Another limitation and source of uncertainty is the lack of a rigorous temperature control, e.g. by a heat controlled water bath, which makes necessary the assumption that the temperature in the central bin equals the temperature of all bins.

Besides the applications mentioned in the introduction, the use of test fluids in a study may allow the investigator to come to a more quantitative experiment, which is beneficial in many regards, e.g. it is beneficial for the application of radiomics or machine learning techniques [57–59], in multi-center studies, for quantitative measures in standardized examinations, and for the definition of cut-off values.

In conclusion, reference curves were presented that can be used to calibrate D_{app} measurements using aqueous PVP solutions at different sample temperatures. This shall enable a more widespread use of PVP solutions as test fluids in phantoms in diffusion weighted imaging experiments.

Supporting information

S1 File. Evaluation of the accuracy of temperature measurements with Luxtron FOT Lab Kit.
(PDF)

S2 File. Separate evaluation for 1.5 T and 3 T.
(DOCX)

S3 File. PVP: Weight per weight & weight per volume.
(XLSX)

S4 File. Assessment of image blurring and Gibbs ringing.
(DOCX)

Acknowledgments

Author Contributions

Conceptualization: FW FBL MEL SB MB.

Formal analysis: FW FBL AMN MEL SB MB.

Funding acquisition: BL.

Investigation: FW FBL AM FM JF KD LL BR MB.

Methodology: FW FBL TAK FM JF KD LL BR MB.

Project administration: FBL MEL MB.

Software: TAK AMN KM-H.

Supervision: FBL MB.

Validation: FW FBL SB MB.

Visualization: FW FBL SB.

Writing – original draft: FW FBL MB.

Writing – review & editing: FW FBL TAK AM FM JF KD LL BR AMN MEL KM-H SB MB.

References

1. Jones DK. Diffusion MRI: Theory, Methods, and Applications: Oxford University Press, New York, USA; 2011.

2. Taouli B, Beer AJ, Chenevert T, Collins D, Lehman C, Matos C, et al. Diffusion-weighted imaging outside the brain: Consensus statement from an ISMRM-sponsored workshop. J Magn Reson Imaging. 2016. https://doi.org/10.1002/jmri.25196 PMID: 26892827.

3. Freitag MT, Bickelhaupt S, Ziener C, Meier-Hein K, Radtke JP, Mosebach J, et al. Selected clinically established and scientific techniques of diffusion-weighted MRI. In the context of imaging in oncology. Der Radiologe. 2016; 56(2):137–47. PMID: 26801187

4. Laun FB, Fritzsche KH, Kuder TA, Stieltjes B. Introduction to the basic principles and techniques of diffusion-weighted imaging. Der Radiologe. 2011; 51(3):170–9. PMID: 21424762

5. Stejskal EO, Tanner JE. Spin diffusion measurements: spin echoes in the presence of a time-dependent field gradient. J Chem Phys. 1965; 42(1):288–92.

6. Basser PJ, Mattiello J, LeBihan D. MR diffusion tensor spectroscopy and imaging. Biophys J. 1994; 66(1):259–67. Epub 1994/01/01. https://doi.org/10.1016/S0006-3495(94)80775-1 PMID: 8130344.

7. Mori S, van Zijl PC. Fiber tracking: principles and strategies—a technical review. NMR in biomedicine. 2002; 15(7–8):468–80. Epub 2002/12/19. https://doi.org/10.1002/nbm.781 PMID: 12489096.

8. Stieltjes B, Kaufmann WE, van Zijl PC, Fredericksen K, Pearlson GD, Solaiyappan M, et al. Diffusion tensor imaging and axonal tracking in the human brainstem. NeuroImage. 2001; 14(3):723–35. PMID: 11506544. https://doi.org/10.1006/nimg.2001.0861

9. Tuch DS. Q-ball imaging. Magn Reson Med. 2004; 52(6):1358–72. PMID: 15562495. https://doi.org/10.1002/mrm.20279

10. Jensen JH, Helpern JA, Ramani A, Lu H, Kaczynski K. Diffusional kurtosis imaging: the quantification of non-gaussian water diffusion by means of magnetic resonance imaging. Magn Reson Med. 2005; 53(6):1432–40. PMID: 15906300. https://doi.org/10.1002/mrm.20508

11. Fieremans E, De Deene Y, Delputte S, Ozdemir MS, Achten E, Lemahieu I. The design of anisotropic diffusion phantoms for the validation of diffusion weighted magnetic resonance imaging. Phys Med Biol. 2008; 53(19):5405–19. https://doi.org/10.1088/0031-9155/53/19/009 PMID: 18765890

12. Fieremans E, De Deene Y, Delputte S, Ozdemir MS, D'Asseler Y, Vlassenbroeck J, et al. Simulation and experimental verification of the diffusion in an anisotropic fiber phantom. J Magn Reson. 2008; 190(2):189–99. https://doi.org/10.1016/j.jmr.2007.10.014 PMID: 18023218

13. Bach M, Fritzsche KH, Stieltjes B, Laun FB. Investigation of Resolution Effects Using a Specialized Diffusion Tensor Phantom. Magn Reson Med. 2014; 71(3):1108–16. https://doi.org/10.1002/mrm.24774 PMID: 23657980

14. Laun FB, Huff S, Stieltjes B. On the effects of dephasing due to local gradients in diffusion tensor imaging experiments: relevance for diffusion tensor imaging fiber phantoms. Magn Reson Imaging. 2009; 27(4):541–8. https://doi.org/10.1016/j.mri.2008.08.011 PMID: 18977104

15. Laun FB, Schad LR, Klein J, Stieltjes B. How background noise shifts eigenvectors and increases eigenvalues in DTI. Magn Reson Mater Phy. 2009; 22(3):151–8. https://doi.org/10.1007/s10334-008-0159-6 PMID: 19067007

16. Hakulinen U, Brander A, Ryymin P, Ohman J, Soimakallio S, Helminen M, et al. Repeatability and variation of region-of-interest methods using quantitative diffusion tensor MR imaging of the brain. Bmc Med Imaging. 2012; 12. Unsp 30 https://doi.org/10.1186/1471-2342-12-30 PMID: 23057584

17. Kasper E, Schuster C, Machts J, Kaufmann J, Bittner D, Vielhaber S, et al. Microstructural White Matter Changes Underlying Cognitive and Behavioural Impairment in ALS—An In Vivo Study Using DTI. Plos One. 2014; 9(12). ARTN e114543 https://doi.org/10.1371/journal.pone.0114543 PMID: 25501028

18. Lorenz R, Bellemann ME, Hennig J, Il'yasov KA. Anisotropic phantoms for quantitative diffusion tensor imaging and fiber-tracking validation. Appl Magn Reson. 2008; 33(4):419–29. https://doi.org/10.1007/s00723-008-0087-7

19. Teipel SJ, Meindl T, Wagner M, Stieltjes B, Reuter S, Hauenstein KH, et al. Longitudinal Changes in Fiber Tract Integrity in Healthy Aging and Mild Cognitive Impairment: A DTI Follow-Up Study. J Alzheimers Dis. 2010; 22(2):507–22. https://doi.org/10.3233/JAD-2010-100234 PMID: 20847446

20. Pullens P, Roebroeck A, Goebel R. Ground Truth Hardware Phantoms for Validation of Diffusion-Weighted MRI Applications. J Magn Reson Imaging. 2010; 32(2):482–8. https://doi.org/10.1002/jmri.22243 PMID: 20677281

21. Farrher E, Kaffanke J, Celik AA, Stocker T, Grinberg F, Shah NJ. Novel multisection design of anisotropic diffusion phantoms. Magn Reson Imaging. 2012; 30(4):518–26. https://doi.org/10.1016/j.mri.2011.12.012 PMID: 22285876

22. Kuder TA, Stieltjes B, Bachert P, Semmler W, Laun FB. Advanced fit of the diffusion kurtosis tensor by directional weighting and regularization. Magnetic Resonance in Medicine. 2012; 67(5):1401–11. https://doi.org/10.1002/mrm.23133 PMID: 22189630

23. Fritzsche KH, Laun FB, Meinzer HP, Stieltjes B. Opportunities and pitfalls in the quantification of fiber integrity: what can we gain from Q-ball imaging? NeuroImage. 2010; 51(1):242–51. https://doi.org/10.1016/j.neuroimage.2010.02.007 PMID: 20149879.

24. Moussavi-Biugui A, Stieltjes B, Fritzsche K, Semmler W, Laun FB. Novel Spherical Phantoms for Q-Ball Imaging Under In Vivo Conditions. Magn Reson Med. 2011; 65(1):190–4. https://doi.org/10.1002/mrm.22602 PMID: 20740652

25. Perrin M, Poupon C, Rieul B, Leroux P, Constantinesco A, Mangin JF, et al. Validation of q-ball imaging with a diffusion fibre-crossing phantom on a clinical scanner. Philos T R Soc B. 2005; 360(1457): 881–91. https://doi.org/10.1098/rstb.2005.1650 PMID: 16087433

26. Rathi Y, Michailovich O, Laun F, Setsompop K, Grant PE, Westin CF. Multi-shell diffusion signal recovery from sparse measurements. Med Image Anal. 2014; 18(7):1143–56. https://doi.org/10.1016/j.media.2014.06.003 PMID: 25047866

27. Bach M, Laun FB, Leemans A, Tax CMW, Biessels GJ, Stieltjes B, et al. Methodological considerations on tract-based spatial statistics (TBSS). Neuroimage. 2014; 100:358–69. https://doi.org/10.1016/j.neuroimage.2014.06.021 PMID: 24945661

28. Fillard P, Descoteaux M, Goh A, Gouttard S, Jeurissen B, Malcolm J, et al. Quantitative evaluation of 10 tractography algorithms on a realistic diffusion MR phantom. NeuroImage. 2011; 56(1):220–34. Epub 2011/01/25. https://doi.org/10.1016/j.neuroimage.2011.01.032 PMID: 21256221.

29. Teipel SJ, Reuter S, Stieltjes B, Acosta-Cabronero J, Ernemann U, Fellgiebel A, et al. Multicenter stability of diffusion tensor imaging measures: A European clinical and physical phantom study. Psychiat Res-Neuroim. 2011; 194(3):363–71.

30. von dem Hagen EAH, Henkelman RM. Orientational diffusion reflects fiber structure within a voxel. Magnet Reson Med. 2002; 48(3):454–9. https://doi.org/10.1002/Mrm.10250 PMID: 12210909

31. Yanasak N, Allison J. Use of capillaries in the construction of an MRI phantom for the assessment of diffusion tensor imaging: demonstration of performance. Magn Reson Imaging. 2006; 24(10):1349–61. https://doi.org/10.1016/j.mri.2006.08.001 PMID: 17145407

32. Yanasak NE, Allison JD, Hu TCC, Zhao Q. The use of novel gradient directions with DTI to synthesize data with complicated diffusion behavior. Med Phys. 2009; 36(5):1875–85. https://doi.org/10.1118/1.3110670 PMID: 19544807

33. Komlosh ME, Ozarslan E, Lizak MJ, Horkay F, Schram V, Shemesh N, et al. Pore diameter mapping using double pulsed-field gradient MRI and its validation using a novel glass capillary array phantom. J Magn Reson. 2011; 208(1):128–35. https://doi.org/10.1016/j.jmr.2010.10.014 PMID: 21084204

34. Benjamini D, Komlosh ME, Basser PJ, Nevo U. Nonparametric pore size distribution using d-PFG: comparison to s-PFG and migration to MRI. J Magn Reson. 2014; 246:36–45. https://doi.org/10.1016/j.jmr.2014.06.017 PMID: 25064269.

35. Delakis I, Moore EM, Leach MO, De Wilde JP. Developing a quality control protocol for diffusion imaging on a clinical MRI system. Phys Med Biol. 2004; 49(8):1409–22. https://doi.org/10.1088/0031-9155/49/8/003 PMID: 15152682

36. Giannelli M, Sghedoni R, Iacconi C, Iori M, Traino AC, Guerrisi M, et al. MR Scanner Systems Should Be Adequately Characterized in Diffusion-MRI of the Breast. Plos One. 2014; 9(1). ARTN e86280 https://doi.org/10.1371/journal.pone.0086280 PMID: 24489711

37. Giannotti E, Waugh S, Priba L, Davis Z, Crowe E, Vinnicombe S. Assessment and quantification of sources of variability in breast apparent diffusion coefficient (ADC) measurements at diffusion weighted imaging. Eur J Radiol. 2015; 84(9):1729–36. https://doi.org/10.1016/j.ejrad.2015.05.032 PMID: 26078100

38. Malyarenko D, Galban CJ, Londy FJ, Meyer CR, Johnson TD, Rehemtulla A, et al. Multi-system repeatability and reproducibility of apparent diffusion coefficient measurement using an ice-water phantom. J Magn Reson Imaging. 2013; 37(5):1238–46. https://doi.org/10.1002/jmri.23825 PMID: 23023785

39. Mulkern RV, Ricci KI, Vajapeyam S, Chenevert TL, Malyarenko DI, Kocak M, et al. Pediatric Brain Tumor Consortium Multisite Assessment of Apparent Diffusion Coefficient z-Axis Variation Assessed with an Ice-Water Phantom. Acad Radiol. 2015; 22(3):363–9. https://doi.org/10.1016/j.acra.2014.10.006 PMID: 25435183

40. Krynicki K, Green CD, Sawyer DW. Pressure and Temperature-Dependence of Self-Diffusion in Water. Faraday Discuss. 1978; 66:199–208. https://doi.org/10.1039/Dc9786600199

41. Holz M, Heil SR, Sacco A. Temperature-dependent self-diffusion coefficients of water and six selected molecular liquids for calibration in accurate H-1 NMR PFG measurements. Phys Chem Chem Phys. 2000; 2(20):4740–2. https://doi.org/10.1039/B005319h

42. Tofts PS, Lloyd D, Clark CA, Barker GJ, Parker GJM, McConville P, et al. Test liquids for quantitative MRI measurements of self-diffusion coefficient in vivo. Magn Reson Med. 2000; 43(3):368–74. https://doi.org/10.1002/(Sici)1522-2594(200003)43:3<368::Aid-Mrm8>3.0.Co;2-B PMID: 10725879

43. Laubach HJ, Jakob PM, Loevblad KO, Baird AE, Bovo MP, Edelman RR, et al. A phantom for diffusion-weighted imaging of acute stroke. Jmri-J Magn Reson Im. 1998; 8(6):1349–54. https://doi.org/10.1002/jmri.1880080627

44. Spees WM, Song SK, Garbow JR, Neil JJ, Ackerman JJH. Use of ethylene glycol to evaluate gradient performance in gradient-intensive diffusion MR sequences. Magn Reson Med. 2012; 68(1):319–24. https://doi.org/10.1002/mrm.23201 PMID: 22127787

45. Zhu T, Hu R, Qiu X, Taylor M, Tso Y, Yiannoutsos C, et al. Quantification of accuracy and precision of multi-center DTI measurements: A diffusion phantom and human brain study. Neuroimage. 2011; 56(3):1398–411. https://doi.org/10.1016/j.neuroimage.2011.02.010 PMID: 21316471

46. Fukuzaki M, Alexander AL, Goodrich C, Hasan K, Buswell HR, Gullberg GT, et al., editors. The ability of Line Scan Diffusion Imaging Method—Comparison with Echo Planner Diffusion Imaging—Proceedings of the 7th Annual Meeting of the ISMRM; 1999; Philadelphia, USA.

47. Horkay F, Pierpaoli C, Basser PJ, inventorsPhantom for diffusion MRI. USA2012.

48. Keenan KE, Wilmes LJ, Aliu SO, Newitt DC, Jones EF, Boss MA, et al. Design of a breast phantom for quantitative MRI. J Magn Reson Imaging. 2016. https://doi.org/10.1002/jmri.25214 PMID: 26949897.

49. Pierpaoli C, Sarlls JE, Nevo U, Basser PJ, Horkay F, editors. Polyvinylpyrrolidone (PVP) water solutions as isotropic phantoms for diffusion MRI studies. Proceedings of the 17th Annual Meeting of the ISMRM; 2009; Honolulu, Hawaii.

50. Pullens P, Bladt P, Parizel P, editors. A highly standardized, easy to produce and cost-effective isotropic PVP diffusion phantom for quality assessment and multi-center studies Proceedings of the 23rd Annual Meeting of the ISMRM; 2015; Toronto, Canada.

51. Chenevert TL, Galban CJ, Ivancevic MK, Rohrer SE, Londy FJ, Kwee TC, et al. Diffusion Coefficient Measurement Using a Temperature-Controlled Fluid for Quality Control in Multicenter Studies. J Magn Reson Imaging. 2011; 34(4):983–7. https://doi.org/10.1002/jmri.22363 PMID: 21928310

52. Keenan KE, Peskin AP, Wilmes LJ, Aliu SO, Jones EF, Li W, et al. Variability and bias assessment in breast ADC measurement across multiple systems. J Magn Reson Imaging. 2016. https://doi.org/10.1002/jmri.25237 PMID: 27008431.

53. Mills R. Self-Diffusion in Normal and Heavy-Water in Range 1–45 Degrees. J Phys Chem-Us. 1973; 77(5):685–8. https://doi.org/10.1021/J100624a025

54. Hellerbach A, Schuster V, Jansen A, Sommer J. MRI Phantoms—Are There Alternatives to Agar? Plos One. 2013; 8(8). ARTN e70343 https://doi.org/10.1371/journal.pone.0070343 PMID: 23940563

55. Benjamini D, Basser PJ. Use of marginal distributions constrained optimization (MADCO) for accelerated 2D MRI relaxometry and diffusometry. Journal of magnetic resonance. 2016; 271:40–5. https://doi.org/10.1016/j.jmr.2016.08.004 PMID: 27543810;

56. Komlosh ME, Benjamini D, Barnett AS, Schram V, Horkay F, Avram AV, et al. Anisotropic phantom to calibrate high-q diffusion MRI methods. J Magn Reson. 2017; 275:19–28. https://doi.org/10.1016/j.jmr.2016.11.017 PMID: 27951427

57. Gillies RJ, Kinahan PE, Hricak H. Radiomics: Images Are More than Pictures, They Are Data. Radiology. 2016; 278(2):563–77. https://doi.org/10.1148/radiol.2015151169 PMID: 26579733

58. Shinohara RT, Sweeney EM, Goldsmith J, Shiee N, Mateen FJ, Calabresi PA, et al. Statistical normalization techniques for magnetic resonance imaging (vol 6, pg 9, 2014). Neuroimage-Clin. 2015; 7:848-. https://doi.org/10.1016/j.nicl.2015.02.011

59. Antunes J, Viswanath S, Rusu M, Valls L, Hoimes C, Avril N, et al. Radiomics Analysis on FLT-PET/MRI for Characterization of Early Treatment Response in Renal Cell Carcinoma: A Proof-of-Concept Study. Translational oncology. 2016; 9(2):155–62. https://doi.org/10.1016/j.tranon.2016.01.008 PMID: 27084432